Volume 13
Number 12
28 March 2025
Pages 8205–8894

Journal of Materials Chemistry A

Materials for energy and sustainability

rsc.li/materials-a

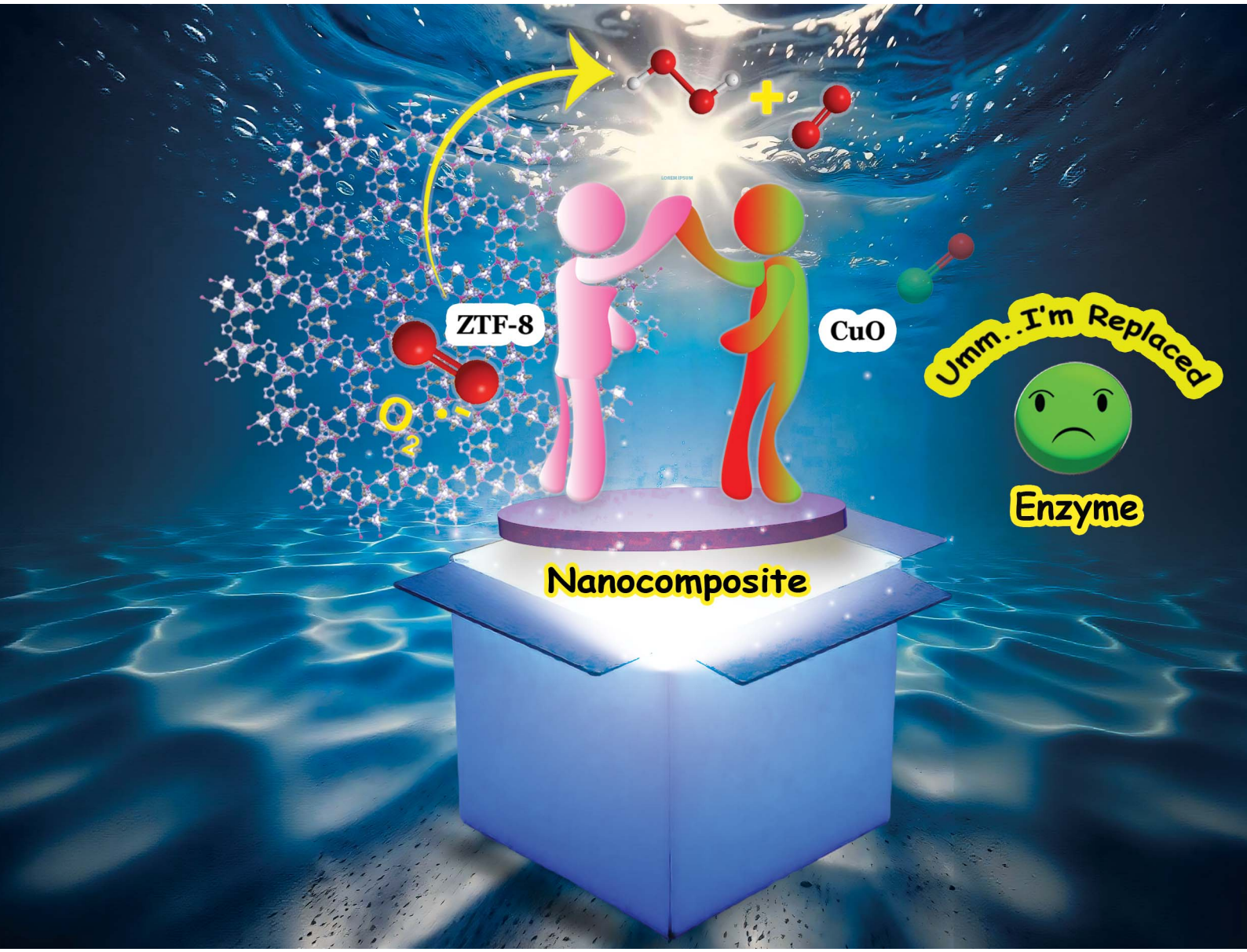

ISSN 2050-7488

ROYAL SOCIETY OF CHEMISTRY

PAPER

Sellappan Senthilkumar *et al.*

Biomimetic CuO/ZTF-8 nanozyme-based neoteric sensor for the selective detection of superoxide anions

Journal of Materials Chemistry A

ROYAL SOCIETY OF CHEMISTRY

PAPER

View Article Online
View Journal | View Issue

Cite this: J. Mater. Chem. A, 2025, 13, 8343

Biomimetic CuO/ZTF-8 nanozyme-based neoteric sensor for the selective detection of superoxide anions†

Vadakke Purakkal Sruthi, ‡[a] Shafeeq Sarfudeen, ‡[a] Tamas Panda, [b] Kathavarayan Thenmozhi [a] and Sellappan Senthilkumar *[a]

Superoxide ($O_2^{\bullet-}$) is a short-lived oxygen intermediate and an inevitable member of the reactive oxygen species, which has been found to participate in several physiological and pathological processes. $O_2^{\bullet-}$ is also well known as a biomarker, as its abnormal levels can lead to tumours and cancers, making its dynamic detection crucial for pathological studies, health screening and early diagnosis of diseases. The rational design of metal–organic frameworks with enzymatic functions has gained increasing interest due to their structural robustness and ability to judiciously introduce numerous active sites into nanosized particles. Herein, for the first time, we have designed and developed a novel copper oxide nanoparticle-embedded zeolitic tetrazolate framework (CuO/ZTF-8) as an enzymatic mimic for the bimetallic enzyme copper–zinc superoxide dismutase (Cu–Zn SOD) and explored its efficacy for the electrochemical detection of $O_2^{\bullet-}$. The constructed sensor displayed linearity for $O_2^{\bullet-}$ detection in two concentration ranges of 25 μM to 350 μM and 350 μM to 2.475 mM, achieving a very low limit of detection of 6.19 μM. The CuO/ZTF-8 demonstrated SOD-like activity due to its structural similarity with natural Cu–Zn SOD and abundant copper active sites. This is also the first-ever report on exploring the ZTF-8 framework through a post-modification approach to accomplish enzyme-mimic activity. The firm anchoring of CuONPs into the ZTF-8 architecture afforded excellent cyclic and long-term stability to the fabricated sensor.

Received 13th October 2024
Accepted 16th December 2024

DOI: 10.1039/d4ta07300b

rsc.li/materials-a

1. Introduction

Superoxide ($O_2^{\bullet-}$) is a potent member of the reactive oxygen species family that plays essential roles in biology and medicine. Under healthy physiological conditions, biological functions, such as generation and apoptosis, are facilitated through the rapid formation and elimination of $O_2^{\bullet-}$. $O_2^{\bullet-}$ exhibits beneficial effects in biological systems when its concentration is 10^{-10} M or lower, while concentrations exceeding this limit may induce oxidative damage and diseases.[1–5] The levels of $O_2^{\bullet-}$ in cells are modulated by the metalloenzyme superoxide dismutase (SOD), which effectively converts $O_2^{\bullet-}$ into H_2O_2 and oxygen (O_2). The four different types of SODs are copper–zinc SOD (Cu–Zn SOD), iron SOD (Fe SOD), manganese SOD (Mn SOD), and nickel SOD (Ni SOD).[6] Among these types, Cu–Zn SOD is of utmost significance due to its presence in the cytosol and extracellular matrix. The impairment of Cu–Zn SOD can escalate the probability of numerous diseases, and as a result, this SOD is considered a potential therapeutic agent.[7] Nevertheless, the strenuous extraction process and the highly sensitive nature of SODs limit their application in various fields of research. Therefore, designing novel materials that mimic the functions of SOD has become an important and urgent necessity.

Ever since the discovery of nanozymes by Yan *et al.* in 2007,[8] they have been explored in different domains, including wound healing, sensing, catalysis and other biomedical applications, due to their advantages, such as high stability, ease of preparation, and recyclability.[9–11] Furthermore, the application of nanozymes that mimic SOD for sensing purposes has gained significant attention only in the past decade.[12] To date, various materials, such as metal oxide nanoparticles,[13] carbon materials,[14] metal–organic frameworks (MOFs),[15] and covalent organic frameworks,[16] have been studied for their ability to

[a]Department of Chemistry, School of Advanced Sciences, Vellore Institute of Technology (VIT), Vellore, Tamil Nadu, 632014, India. E-mail: senthilanalytical@gmail.com; senthilkumar.s@vit.ac.in

[b]Centre for Clean Environment (CCE), Vellore Institute of Technology, Vellore (VIT), Tamil Nadu, 632014, India

† Electronic supplementary information (ESI) available: Materials and instrumentation details, UV-vis spectrum and PXRD pattern of CuONP, HRTEM, size distribution curve, SAED pattern of CuONP, FESEM and elemental mapping of CuO/ZTF-8 nanocomposite, XPS survey spectrum and O 1s spectrum of CuO/ZTF-8 nanocomposite, absorbance spectra of KO_2, ESR of $O_2^{\bullet-}$, effect of pH, EIS, effect of scan rate, PXRD patterns before and after electrochemical sensing, amperometric curves obtained during real sample analysis. See DOI: https://doi.org/10.1039/d4ta07300b

‡ The authors have contributed equally towards this work.

mimic enzymatic functions. Among the aforementioned materials, MOFs are gaining significant attention due to their remarkable properties, such as tailorable structure and morphology, greater surface area, and high stability.[17] The structure and morphology of MOFs can be prudently tuned by incorporating metal nanoparticles or encapsulating biomacromolecules.[18] Notably, a few of these MOFs have been reported to function as SOD mimetics and have been successfully utilized for the detection of significant analytes.[19,20] In particular, the zeolitic imidazole framework (ZIF-8) with a sodalite topology has been widely investigated for sensing applications[21–23] due to its ease of synthesis, exceptional stability, and high porosity. Recently, scientists discovered that tetrazole could also form μ_2-bridging coordination bonds with tetrahedral metal centres, similar to imidazolate-based ZIFs with two uncoordinated N-heteroatom sites to form a series of four linked porous frameworks known as zeolitic tetrazolate frameworks (ZTFs). These ZTFs have recently been used for gas sorption, catalysis, and to a small extent in sensing. Hence, there is a broad scope for developing these kind of frameworks as sensor materials.[24–27] There exists a fundamental distinction between coordination cages, *i.e.* MOFs, ZIFs, and ZTFs. Coordination cages exhibit isolated structures, whereas in ZIFs and ZTFs, the cages are covalently interconnected with neighbouring cages. Furthermore, coordination cages generally comprise uncharged pyridyl linkers, whereas ZIFs and ZTFs are constructed using charged imidazolate and tetrazolate linkers, which accounts for their impressive thermal, chemical, and architectural stabilities. The interconnected vertices of extended structures constructed *via* fused cages provide high chemical and architectural stabilities. Additionally, the ability to connect a diverse array of cages with varying chemical environments in closely confined spaces provides a well-defined spatial arrangement. Copper oxide nanoparticles (CuONPs) are well known for their excellent conductivity, electrocatalytic activity, eco-friendly nature, and stability, due to which they have been utilized in disparate fields of electrochemistry.[28] CuONP-based nanocomposites have also been proven to exhibit better conductivity and stability because of the synergistic effect between the CuONPs and the substrate.[29] Hence, we aimed to synthesize a novel nanocomposite by making use of the traditional CuONPs and the still blooming ZTF-8, which we believed would result in a wide range of potentialities and prospects within the relatively uncharted domain of reticular chemistry between ZTF and nanoparticles.

In the family of ZTFs, our recently reported ZTF-8, which also adopts a similar sodalite topology to that of ZIF-8, is still finding blooming potential in sensing applications.[30] The judicious combination of CuONPs and ZTF-8 could act as a functional mimic for the bimetallic Cu–Zn SOD enzyme. This motivated us to develop a novel nanocomposite sensing platform, consisting of CuONPs and ZTF-8, towards the electrochemical detection of $O_2^{\bullet-}$. The thus-obtained nanocomposite was drop-cast on a glassy carbon electrode (GCE) to develop a CuO/ZTF-8/GCE and this fabricated sensor was employed to detect $O_2^{\bullet-}$ amperometrically at an operating potential of −0.2 V. The sensor exhibited a good dynamic range and low detection limit along with excellent selectivity and sensitivity towards the detection of $O_2^{\bullet-}$.

2. Experimental section

All the chemicals and instrumentation details are given in the ESI.†

2.1 Synthesis of copper oxide nanoparticles

Copper oxide nanoparticles (CuONPs) were synthesized by slightly modifying a procedure reported earlier.[31] Initially, 60 mL ethanolic solution consisting of 2.0 g of copper acetate was stirred for 20 min, followed by the addition of 0.6 g of sodium hydroxide. The obtained solution was then transferred into a 100 mL Teflon-lined autoclave and kept at a temperature of 120 °C for 2 h. After completion of this process, the reaction mixture was cooled to room temperature to yield a blackish brown precipitate that was carefully washed several times using ethanol and then subjected to drying at 80 °C in a vacuum oven to attain the final desired CuONPs.

2.2 Synthesis of ZTF-8

ZTF-8 was synthesized in a Fritsch ball mill using a liquid-assisted grinding approach at room temperature.[32] Herein, 3.68 mmol of zinc oxide (ZnO) and 7.13 mmol of 5-methyl tetrazole (5-mtz) were blended in a stainless-steel milling jar with 30–40 μL of methanol, followed by the addition of 6 stainless-steel balls. The mixture was then ground for 1 h and 30 min at 100 rpm. After completion of the milling, the sample was washed multiple times with ethanol and dried in a high vacuum at 120 °C overnight to obtain the final ZTF-8 product.

2.3 Synthesis of CuO/ZTF-8

The optimized procedure for the synthesis of the CuO/ZTF-8 nanocomposite is illustrated in Scheme 1. Specifically, ZTF-8 and CuONP (1 : 1 wt%) were dispersed in 15 mL of *N*,*N*-dimethyl formamide (DMF), to which 4 mL ammonia solution was added and the mixture was stirred for 24 h in an inert atmosphere (N_2) at 90 °C. Thereafter, the obtained black suspension was cooled to room temperature. Later, the compound was washed initially with DMF to remove the impurities and further washed with ethanol and dried in a vacuum oven at 90 °C to yield the CuO/ZTF-8 nanocomposite.

2.4 Fabrication of the CuO/ZTF-8 nanocomposite-modified electrode

A glassy carbon electrode (GCE) was polished in slurries of alumina powder of various sizes (1 micron, 0.5 micron, and 0.05 micron) and sonicated in a 1 : 1 ethanol–water mixture to obtain a clean GCE. Then, the catalyst ink was prepared by thoroughly mixing 5 mg of CuO/ZTF-8 nanocomposite in 250 μL ethanol, 245 μL H_2O and 5 μL Nafion. Next, 10 μL of this catalyst ink was drop-cast onto the precleaned working electrode at ≈25 °C to obtain the CuO/ZTF-8/GCE-modified electrode. Before conducting the electrochemical investigations, the CuO/ZTF-8/GCE

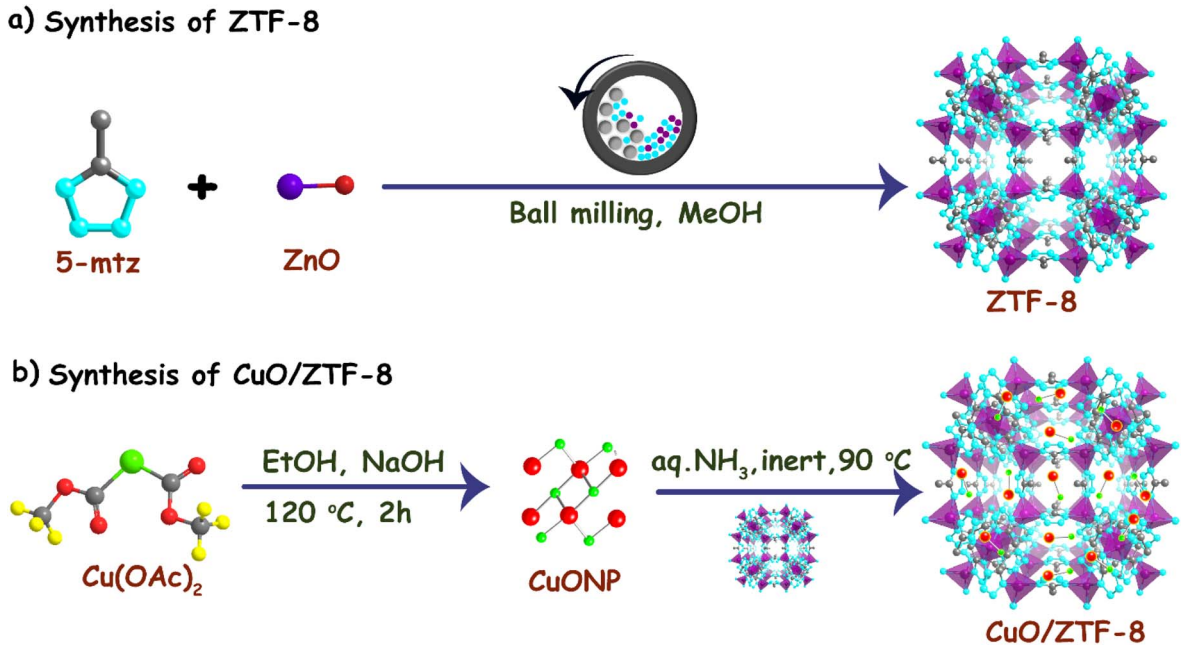

Scheme 1 Schematic of the synthesis of (a) ZTF-8, (b) CuONP and CuO/ZTF-8 nanocomposite.

was subjected to potential cycles in the range of −0.4 to +0.4 V. Other electrodes, namely CuONP-modified GCE (CuO/GCE) and ZTF-8-modified GCE (ZTF-8/GCE), were also prepared in a similar manner for comparison.

3. Results and discussion

3.1 Characterization of the CuO/ZTF-8

Initially, the synthesized CuONPs were characterized using UV-vis spectroscopy and high-resolution transmission electron microscopic (HRTEM). The UV-vis spectrum of the CuONP (Fig. S1a†) exhibited the characteristic peak of CuO at 295 nm, evidencing its successful formation.[33] The HRTEM images of the CuONP is demonstrated in Fig. S2a† and the size-distribution curve portrayed that the size of the CuONPs was around 5 nm (Fig. S2b†). Also, the *d*-spacing lines in Fig. S2c† corresponded to the (111) plane of the CuONPs, and the selected area electron diffraction (SAED) pattern in Fig. S2d† proves the high crystallinity of the CuONPs. Further, the crystallinity of the synthesized CuONPs, ZTF-8, and CuO/ZTF-8 nanocomposite was characterized using powder X-ray diffraction (PXRD) and the resultant patterns are displayed in Fig. 1a. The PXRD pattern of the CuONPs (blue) showed peaks at 32.2° (110), 35.3° (002), and 38.6° (111), which matched well with JCPDS No: 48-1548, indicating the absence of other possible impurities, such as $Cu(OH)_2$ (Fig. S1b†).[31] Further, the PXRD pattern of ZTF-8 (green) revealed peaks at 7.8° (011), 10.5° (002), 12.9° (112), 15.0° (022), 16.7° (013), and 21.6° (222), consistent with our previously reported PXRD pattern of ZTF-8.[30] Moreover, the diffraction pattern of CuO/ZTF-8 (brown) exhibited characteristic peaks of both the CuONPs and that of ZTF-8, denoting the successful formation of the CuO/ZTF-8 nanocomposite.

Field emission scanning electron microscopy (FESEM) and HRTEM were used to examine the morphology of the synthesized CuO/ZTF-8 nanocomposite (Fig. S3† and 1b and c, respectively). From the figures (Fig. 1b and S3†), it is evident that the CuO/ZTF-8 nanocomposite adopted a defective square morphology. The *d*-spacing value was found to be 0.23 nm from Fig. 1c, which corresponds to the (111) plane of CuONPs. The SAED pattern in Fig. 1d shows the highly crystalline nature of the CuO/ZTF-8 nanocomposite and the results were found to be consistent with the obtained PXRD spectrum, confirming the successful formation of the nanocomposite. Further, the elemental mapping of CuO/ZTF-8 in Fig. S3† revealed that the elements, Zn, Cu, C, N, and O were uniformly distributed throughout the nanocomposite.

The surface composition of the synthesized CuO/ZTF-8 nanocomposite was determined using X-ray photoelectron spectroscopy, where the survey spectrum (Fig. S4a†) revealed the presence of copper (Cu), zinc (Zn), oxygen (O), nitrogen (N), and carbon (C). Fig. S4b† presents the deconvoluted O 1s spectrum, where the peak at a binding energy (BE) value of 529.13 eV could be attributed to the Cu=O and the peak at 530.65 eV could be due to the presence of intrinsic oxygen defects in the crystal lattice.[34] The core-level spectrum of Zn 2p (Fig. 2a) displayed two sturdy peaks with BEs of 1044.6 and 1021.9 eV ascribed to Zn $2p_{1/2}$ and Zn $2p_{3/2}$.[35] The N 1s spectrum was deconvoluted into four individual peaks at 398.8, 399.4, 400.1, and 400.7 eV, ascribed to Zn–N,[36] N=C,[30] N=N–N,[37] and N–C,[38] respectively (Fig. 2b). The C 1s spectrum shown in Fig. 2c displayed three separate peaks at 284.2, 285.5, and 287.3 eV, which corresponded to C–C, C–N, and C=N bonds,[38] respectively. Further, the two peaks at BE values of 953.0 and 932.9 eV accompanied by two strong satellite peaks around 941 and

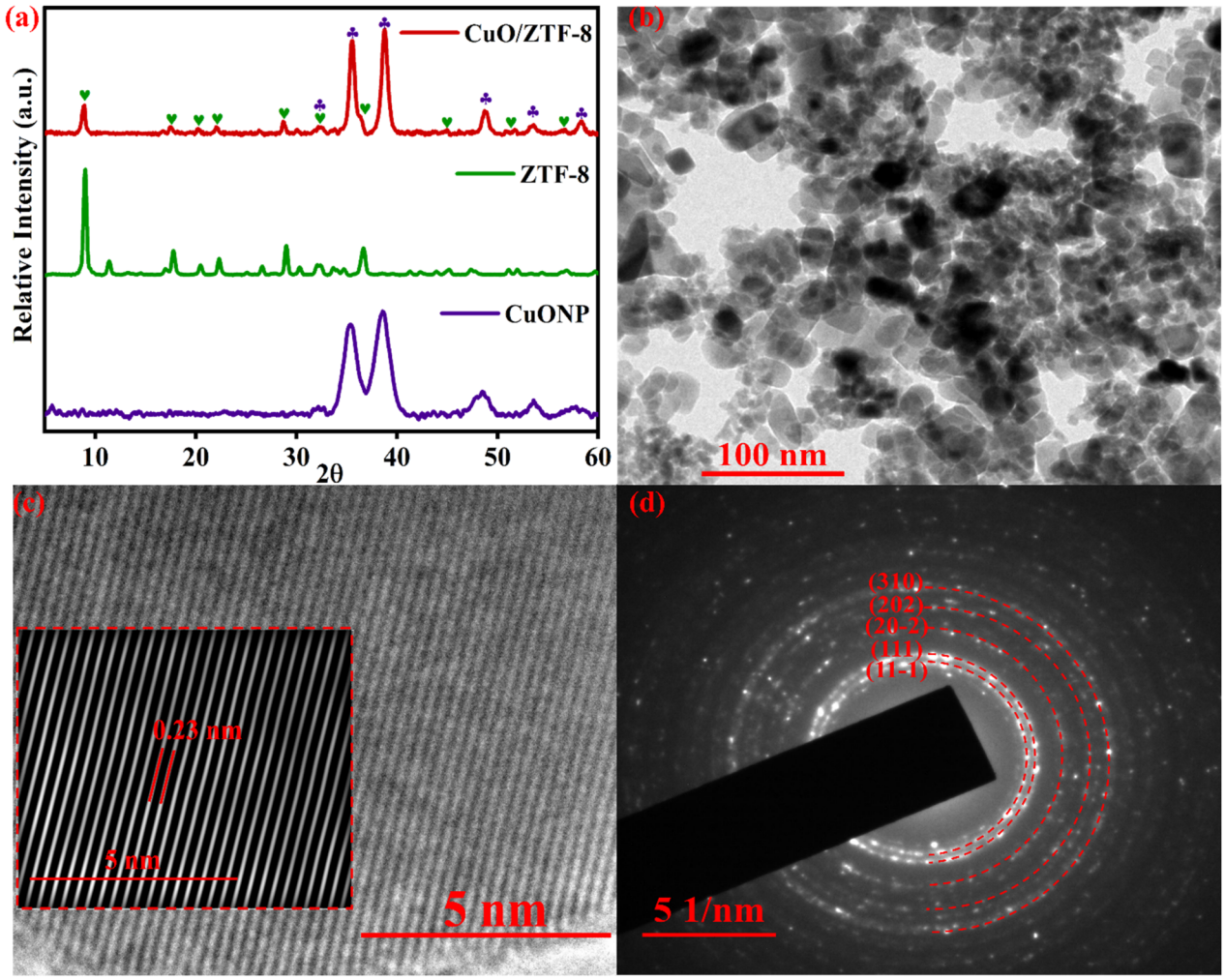

Fig. 1 (a) PXRD spectra of CuONP (blue), ZTF-8 (green), and CuO/ZTF-8 (brown), (b and c) HRTEM images and (d) SAED pattern of the CuO/ZTF-8 nanocomposite.

961 eV in the core-level spectrum of Cu 2p (Fig. 2d) could be attributed to the $2p_{1/2}$ and $2p_{3/2}$ of Cu^{2+}, respectively.[34,39]

3.2 Superoxide mimicking activity of the CuO/ZTF-8 nanocomposite

The CuO/ZTF-8 nanocomposite was prudently designed as a functional mimic of Cu–Zn SOD and thus the SOD-mimicking activity of the synthesized nanocomposite was probed initially. Typically, $O_2^{\bullet-}$ was generated by ultrasonicating 7.1 mg of KO_2 in DMSO in the presence of 52.8 mg of 18-crown-6, which was confirmed by the characteristic absorbance peak of $O_2^{\bullet-}$ at 271 nm (Fig. S5†). The generation of $O_2^{\bullet-}$ was next investigated using (2,2,6,6-tetramethylpiperidin-1-yl)oxyl (TEMPO) as the SOD analogue ($O_2^{\bullet-}$ scavenger)[40] and the results are presented in Fig. S6.† TEMPO consists of a stable nitroxide radical that exhibits a triplet in the ESR spectrum, which can be used as spin labels for ESR studies. The *g*-value of TEMPO was found to be 2.0015 and this corresponds to the stable nitroxide radical (Fig. S6a†). Fig. S6b† demonstrates the ESR spectra of 0.1 mM of TEMPO in DMSO in the presence and absence of $O_2^{\bullet-}$. Strong ESR signals corresponding to nitroxide radicals could be observed in the absence of $O_2^{\bullet-}$ (blue curve), which were completely subsided in the presence of $O_2^{\bullet-}$ (red curve). The disappearance of the ESR signals was due to the conversion of all the nitroxide radicals into hydroxylamine in the presence of $O_2^{\bullet-}$. Thus, the formation of $O_2^{\bullet-}$ was successfully demonstrated in the ESR studies.

Further, the biomimetic characteristics can be comprehended by studying the disproportion of $O_2^{\bullet-}$ in the presence of nitroblue tetrazolium (NBT), which acts as an $O_2^{\bullet-}$ indicator. In the absence of any enzyme or catalyst, $O_2^{\bullet-}$ could eventually reduce NBT to a blue-violet-coloured compound, namely formazan (exhibiting an absorbance peak at 540 nm). However, in the presence of an enzyme/catalyst, all the $O_2^{\bullet-}$ will not be available for the conversion of NBT to formazan. Fig. 3a reveals the absorbance spectra of $O_2^{\bullet-}$ and NBT in the presence and absence of CuO/ZTF-8. In Fig. 3b, in the presence of either CuONP (blue curve) or ZTF-8 (green curve), an absorbance peak was observed at 540 nm corresponding to the reduction of NBT to formazan by $O_2^{\bullet-}$, indicating that neither CuO nor ZTF-8

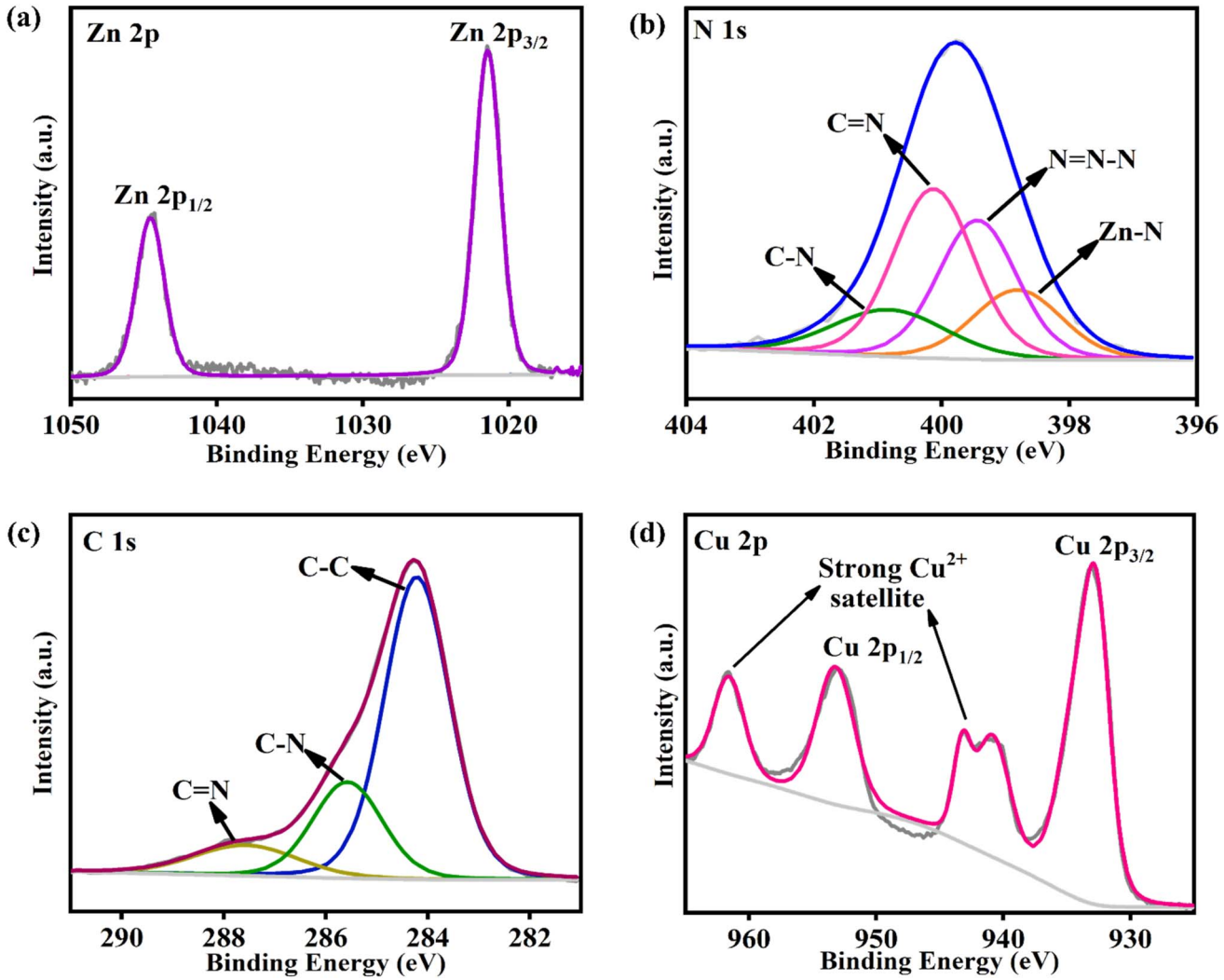

Fig. 2 Core-level XPS spectra of (a) Zn 2p, (b) N 1s, (c) C 1s, and (d) Cu 2p of the CuO/ZTF-8 nanocomposite.

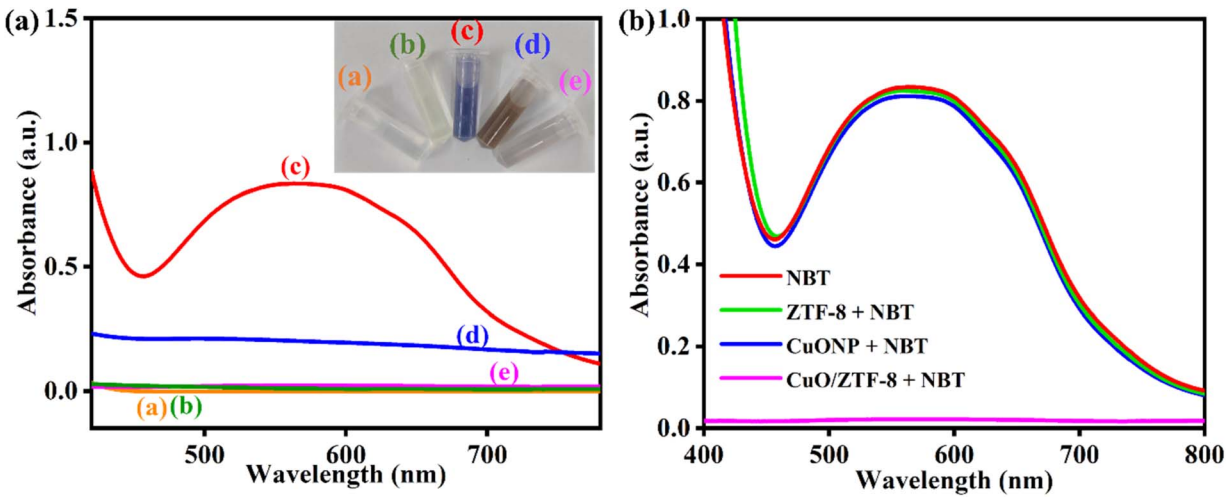

Fig. 3 Absorbance spectra of (a) $O_2^{\bullet-}$ in DMSO (orange), (b) 1 mg mL^{-1} of NBT in 0.1 M PBS (pH 7) (green), (c) $O_2^{\bullet-}$–NBT system (red), (d) 0.5 mg mL^{-1} of CuO/ZTF-8 in 0.1 M PBS (pH 7) (blue), and (e) $O_2^{\bullet-}$–NBT system in the presence of CuO/ZTF-8 (pink). (Inset) Visual representation of the colour changes observed (b) $O_2^{\bullet-}$–NBT system in the absence (red) and presence of ZTF-8 (green), CuONP (blue), and CuO/ZTF-8 (pink) in 0.1 M PBS (pH 7).

could act as an SOD mimetic. Meanwhile, upon the addition of CuO/ZTF-8, the peak at 540 nm corresponding to formazan disappeared, proving the ability of CuO/ZTF-8 to act as an $O_2^{\bullet-}$ scavenger and thus demonstrating its SOD-mimicking activity. These results elucidate that the Cu–Zn SOD-mimicking activity was attained due to the judicious choice of CuO and ZTF-8 for the preparation of the nanocomposite.

3.3 Electrocatalytic behaviour of the CuO/ZTF-8/GCE

The promising SOD activity of the CuO/ZTF-8 nanocomposite established in the UV-vis investigations motivated us to further explore its electrocatalytic performance. Initially, the electrochemical responses of bare GCE, ZTF-8/GCE, CuO/GCE, and CuO/ZTF-8/GCE were examined by performing cyclic voltammetry (CV) studies in 0.1 M PBS (pH 7; N_2 saturated) at a scan rate of 50 mV s^{-1} and the results are portrayed in Fig. 4a. As anticipated, the cyclic voltammograms of bare GCE (black curve) and ZTF-8 (green curve) did not portray any redox peaks, whereas the CuO/GCE exhibited redox peaks with cathodic and anodic peak potentials at −0.102 and +0.022 V, correspondingly, with this set of redox peaks due to the $Cu^{2+/+}$ redox couple. Meanwhile, the CuO/ZTF-8/GCE (red curve) displayed well-defined redox peaks with cathodic and anodic potentials at −0.030 and +0.028 V, correspondingly. It was interesting to observe that the CuO/ZTF-8/GCE demonstrated distinct redox peaks with a higher peak current and lesser peak separation (124 mV for CuO/GCE and 58 mV for CuO/ZTF-8/GCE), evidencing that ZTF-8 could act as a versatile platform for the formation of the nanocomposite with enhanced electrochemical properties. The effect of pH on the electrochemical behaviour of the CuO/ZTF-8 nanocomposite-modified electrode was tested in the pH range of 4–10 (Fig. S7a and b†). No redox response could be observed at pH 4, whereas a feeble redox peak was noticed at pH 5. When the pH was further increased to 6, a better redox behaviour was observed, and the peak currents reached the maximum when the pH was increased up to 7. It could be observed from the figures that further increasing the pH resulted in a declining redox response and thus pH 7 was chosen as the optimum pH for the further electrochemical investigations. The conductivity of the individual components

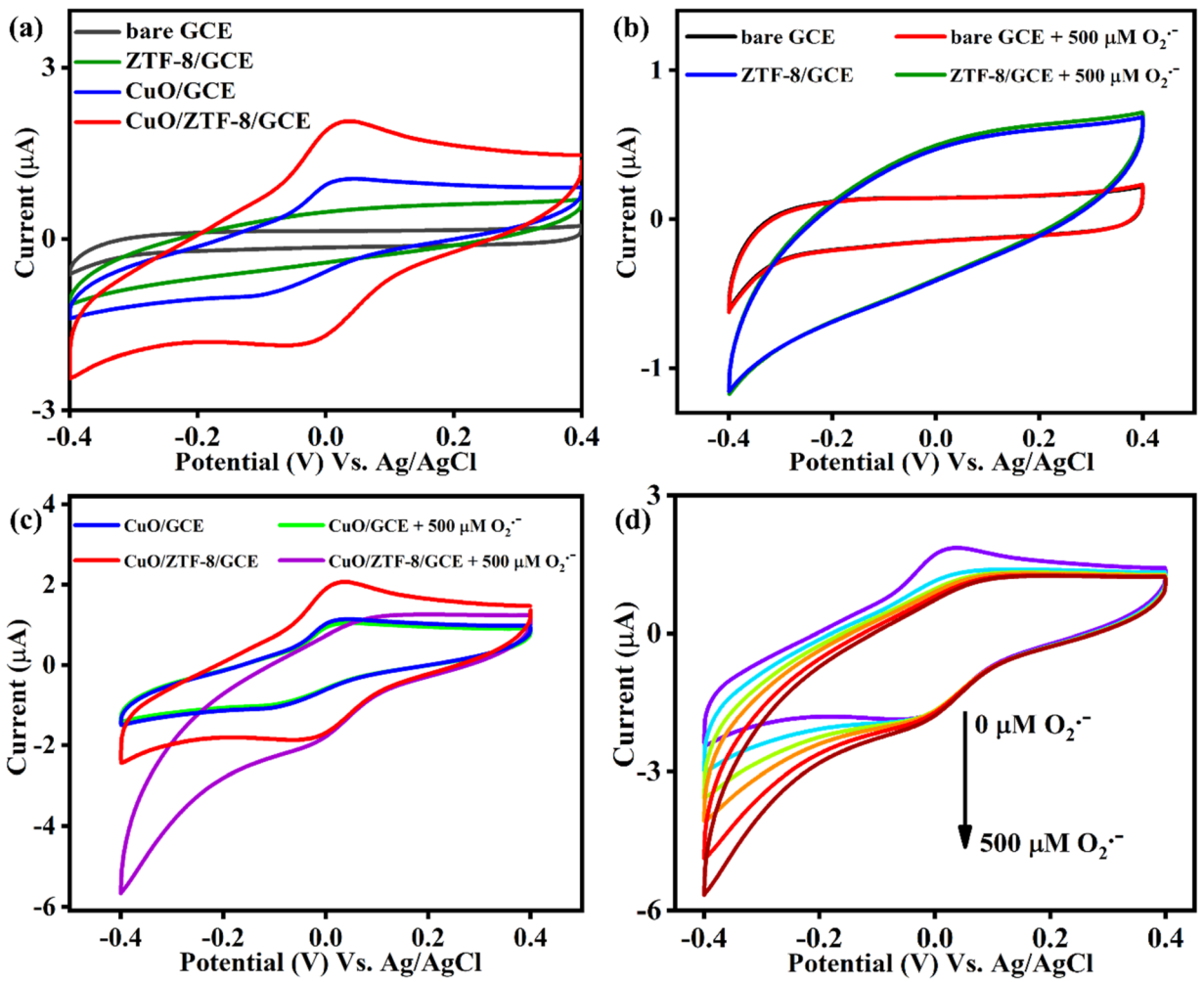

Fig. 4 (a) CV curves of bare GCE, ZTF-8/GCE, CuO/GCE, and CuO/ZTF-8/GCE. (b and c) Electrocatalytic activities of bare GCE, ZTF-8/GCE, CuO/GCE, and CuO/ZTF-8/GCE in the absence and presence of 500 μM $O_2^{\bullet-}$ (d) Electrocatalytic response of CuO/ZTF-8/GCE for successive additions of 100 μM $O_2^{\bullet-}$ (electrolyte: N_2-saturated 0.1 M PBS (pH 7)).

used for the fabrication of the sensor were compared using electrochemical impedance spectroscopy (EIS) (Fig. S8†). The EIS studies were performed in 5 mM $[Fe(CN)_6]^{3-}$ and the diameter of the semi-circles obtained from the corresponding Nyquist plot revealed the charge-transfer resistance (R_{ct}). The bare GCE, CuO/GCE, ZTF-8/GCE, and CuO/ZTF-8/GCE displayed R_{ct} values of 717, 229, 204, and 142 Ω, respectively. The lowest R_{ct} was obtained with the CuO/ZTF-8/GCE, indicative of a high conductivity and faster electron transport upon the formation of the CuO/ZTF-8 heterostructure, which in turn would enhance the electrocatalytic performance. Further, the effect of the scan rate for CuO/ZTF-8/GCE was also studied utilizing CV at different scan rates, as presented in Fig. S9a.† The oxidation and reduction peaks exhibited a gradual increase in peak current upon increasing the scan rate. A linear plot was obtained for the scan rate *versus* peak current, as displayed in Fig. S9b,† revealing that the redox process occurring at the surface of the modified electrode was surface-controlled.

The integration of CuONPs and ZTF-8 could be expected to result in the formation of heterostructures, which in turn would afford a larger number of catalytically active sites. The generation of catalytically active sites could be understood by comparing the electrochemical active surface area (ECSA) of the CuO/GCE, ZTF-8/GCE, and CuO/ZTF-8/GCE, while the ECSA could be obtained using the Randles–Sevcik equation,[41–43] as displayed below:

$$i_p = 2.69 \times 10^5 \times A \times C \times n^{3/2} \times D^{1/2} \times v^{1/2}$$

where i_p (A) is the anodic peak current, A (cm^2) is the ECSA, C (mol cm^{-3}) is the concentration of Fe^{3+} ions, n is the number of electrons involved in the redox process, D (cm^2 s^{-1}) is the diffusion coefficient of Fe^{3+}, and v (V s^{-1}) is the scan rate. The ECSA was obtained from the slope of the square root of the scan rate *vs.* the current and was calculated to be 0.416 cm^2 for CuO/ZTF-8/GCE, 0.186 cm^2 for CuO/GCE, and 0.103 cm^2 for ZTF-8/GCE. The dramatically higher ECSA value of CuO/ZTF-8/GCE compared to CuO/GCE and ZTF-8/GCE clearly evidenced the formation of a heterostructure with a larger number of catalytically active sites.

Since a distinct redox behaviour was observed with the CuO/ZTF-8 heterostructure, we further explored its electrocatalytic activity towards the reduction of $O_2^{\bullet-}$. The voltammetric responses of the bare, ZTF-8/GCE, CuO/GCE, and CuO/ZTF-8/GCE were tested in the presence of 500 μM of $O_2^{\bullet-}$ and the results are displayed in Fig. 4b and c. As expected, the bare and ZTF-8 (Fig. 4b)-modified GCEs did not show any prominent response in the absence or presence of $O_2^{\bullet-}$, demonstrating that neither could show any catalytic activity towards $O_2^{\bullet-}$. Though the CuO/GCE (Fig. 4c) showed a redox peak, it did not show any response upon the addition of $O_2^{\bullet-}$, evidencing that the CuONPs were not catalytically active in the absence of ZTF-8. Furthermore, the CuO/ZTF-8/GCE was also tested for its ability towards the electrocatalytic reduction of $O_2^{\bullet-}$, where it displayed a prominent increase in cathodic current with a decrease in anodic current in the presence of 500 μM of $O_2^{\bullet-}$. This in turn substantiated that the CuO/ZTF-8 nanocomposite obtained by the discrete selection of CuONPs and ZTF-8 could act as a Cu–Zn SOD mimetic and could be employed for the electrochemical detection of $O_2^{\bullet-}$. Additionally, the electrocatalytic activity of the CuO/ZTF-8/GCE was probed using CV in 0.1 M PBS (pH 7, N_2 saturated), whereby it displayed an increase in the cathodic current upon the successive additions of $O_2^{\bullet-}$ (Fig. 4d). This excellent electrocatalytic response was obtained due to the prudent choice of CuO and ZTF-8 for the fabrication of the CuO/ZTF-8/GCE.

3.4 Amperometric detection of $O_2^{\bullet-}$

The eminent electrocatalytic activity of CuO/ZTF-8/GCE towards the reduction of $O_2^{\bullet-}$ inspired us to inspect its analytical performance using amperometry under dynamic conditions in 0.1 M PBS (pH 7, N_2 saturated). The amperometric response was recorded at various applied potentials for the sequential addition of 25 μM of $O_2^{\bullet-}$, which was carried out by spiking 25 μL of 10 mM KO_2 solution in to 10 mL PBS buffer (Fig. 5a). The fabricated sensor did not show any response when the applied potential was 0 V (pink). Though it displayed an increase in cathodic current at an applied potential of −0.1 V (green), the sensor had a higher response time and also lost its ability to sense $O_2^{\bullet-}$ at higher concentrations. Further, the sensor was tested for its ability to detect $O_2^{\bullet-}$ at operating potentials of −0.2 V (blue) and −0.3 V (yellow). Remarkably, the CuO/ZTF-8/GCE disclosed excellent electrocatalytic activity, with a linear current response at an applied potential of −0.2 V. Though the sensor was able to exhibit reasonable activity at an applied potential of −0.3 V, the obtained response was non-linear and inconsistent, and hence −0.2 V was fixed as the operating potential of the sensor in the further amperometric investigations. Fig. 5b displays the amperometric response of CuO/ZTF-8/GCE with increasing concentrations of $O_2^{\bullet-}$ spiked at intervals of 25 s. It is noteworthy to mention that the fabricated sensor displayed a rapid detection time of less than 1 s. The corresponding calibration plot (Fig. 5c) has two concentration ranges between 25–350 μM and 350 μM to 2.475 mM with corresponding sensitivities of 0.039 and 0.023 μA μM^{-1} cm^{-2} and a limit of detection (LOD) as low as 6.19 μM. The analytical performance attained with the CuO/ZTF-8/GCE sensor was also compared with some previously reported electrochemical sensors for the detection of $O_2^{\bullet-}$ and this comparison is shown in Table 1. The results attained with the CuO/ZTF-8/GCE were either better or comparable with most of the recent reports. The consistent catalytic current response obtained with the CuO/ZTF-8/GCE sensor illustrated the prodigious SOD-mimicking nature of the constructed sensor attained due to the deliberate choice of CuO and ZTF-8 for the formation of the nanocomposite. Two plausible sensing mechanisms for the detection of $O_2^{\bullet-}$ are speculated as follows:[54,55].

$$Cu^{2+} + O_2^{\bullet-} \rightarrow Cu^{+} + O_2 \quad \text{(i)}$$

$$Cu^{+} + O_2^{\bullet-} + H_2O \rightarrow Cu^{2+} + H_2O_2 \quad \text{(ii)}$$

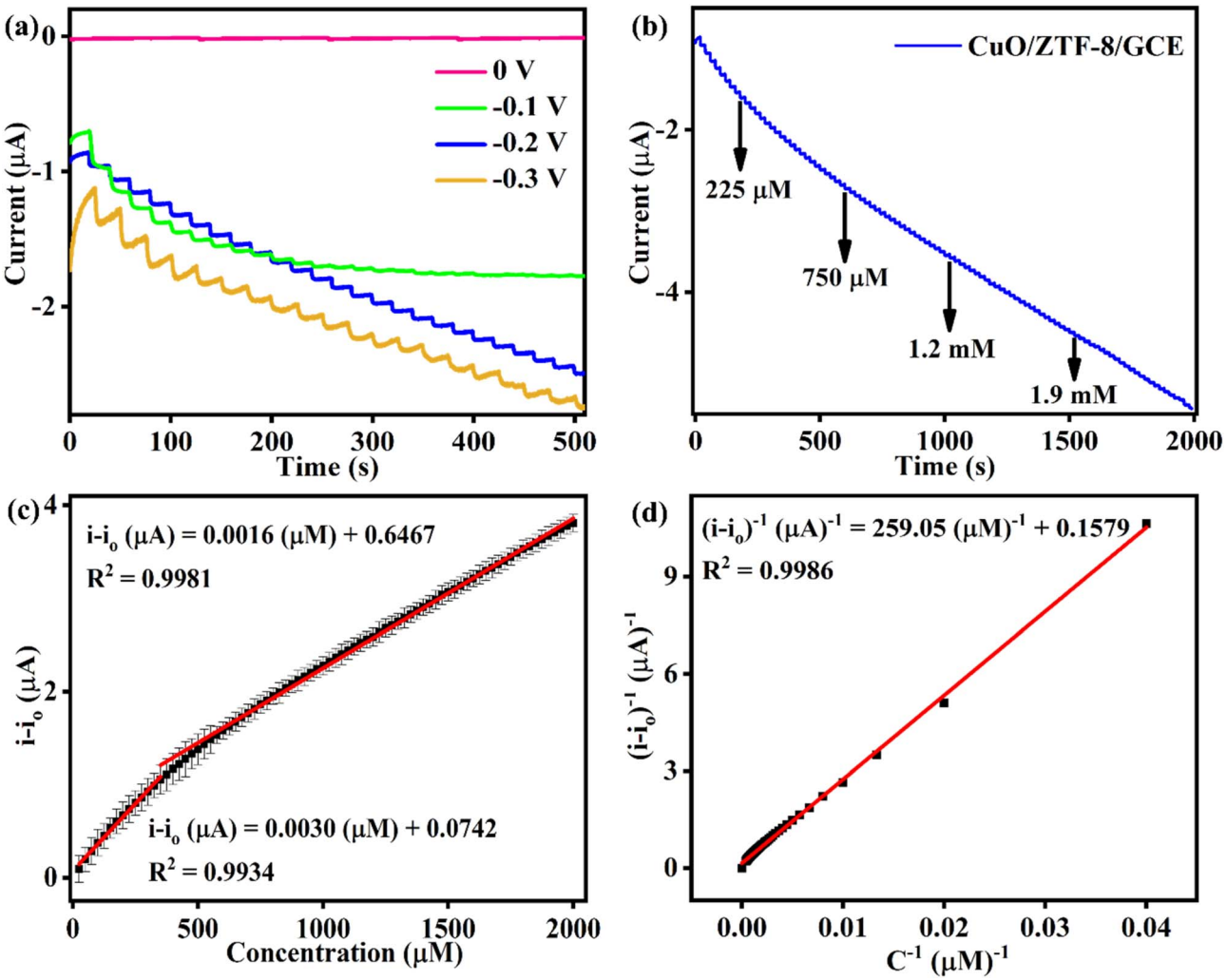

Fig. 5 (a) Amperometric response of CuO/ZTF-8/GCE for the successive addition of $O_2^{\bullet-}$ in N_2-saturated 0.1 M PBS (pH 7) at applied potentials of 0 V (pink), −0.1 V (green), −0.2 V (blue), and −0.3 V (yellow). (b) Amperometric response of CuO/ZTF-8/GCE for the successive addition of $O_2^{\bullet-}$ at an applied potential of −0.2 V. (c) Corresponding calibration plot. (d) Lineweaver–Burk plot for the CuO/ZTF-8 nanocomposite obtained from the amperometric responses.

Table 1 Comparative analytical performances of some reported electrochemical superoxide sensors and the present work

S. no.	Electrode material	Operating potential (V)	Linear range (μM)	LOD (μM)	Sensitivity	Ref.
1	Gelatin–Cu–Zn–SOD/PtSPE	—	100–100000	0.31	—	44
2	Pt–Pd/MWCNTs/SPGE	−0.1	40–1550	0.71	0.601 mA mM^{-1} cm^{-2}	45
3	ELM-12 NS/LIG	−0.1	10–1200	3.01	0.01414 μA mM^{-1} cm^{-2}	46
4	HPCN/SPCE	−0.5	0–338 338–1098	0.615	607.4 μA mM^{-1} cm^{-2}	47
5	AgNPs/SDSMWCNTs/GCE	−0.5	0.000269–0.276 0.669–268	0.00009	—	48
6	SOD/GNPs-CS-IL/GCE	−0.15	0.0056–0.0027	0.0017	—	49
7	SOD/SA/AuE	0	0.44–229.88	0.23	0.00078 A μM^{-1} cm^{-2}	50
8	SOD/AuE	+0.3 & −0.2	13–130 nM min^{-1}	6 nM min^{-1}	—	51
9	MnCo-LDH/ZIF	+0.85	0.0015–10	0.0008	439.2 μA μM^{-1} cm^{-2}	20
10	CTS-$Mn_3(PO_4)_2$chip	+0.7	0.0579–5	0.0094	1.6 μA μM^{-1}	52
11	Mn-MPSA-MWCNT/SPCE	+0.7	0–1817	0.127	77.47 μA mM^{-1} cm^{-2}	53
12	**CuO/ZTF-8/GCE**	**−0.2**	**25–350** **350–2475**	**6.19**	**0.039 μA μM^{-1}cm^{-2}**	**This work**

The first mechanism is expected to proceed by a two-step process. The initial step (i) involves the reduction of Cu^{2+} present in the CuO/ZTF-8 to Cu^{+} and a subsequent oxidation of $O_2^{\bullet-}$ to oxygen. In the second step (ii), the Cu^{+} further reacts with another molecule of $O_2^{\bullet-}$ in the presence of water to yield H_2O_2 followed by the reoxidation of Cu^{+} to Cu^{2+}. The second mechanism can be expressed as follows:

$$Cu^{2+} + O_2^{\bullet-} \rightarrow Cu^{2+} - O_2^{\bullet-} \quad \text{(iii)}$$

$$Cu^{2+} - O_2^{\bullet-} + O_2^{\bullet-} + H_2O \rightarrow Cu^{2+} + O_2 + H_2O_2 \quad \text{(iv)}$$

The second feasible mechanism also takes place *via* a two-step process. In the first step (iii), a superoxide complex is formed between CuO and $O_2^{\bullet-}$, which then reacts with another molecule of $O_2^{\bullet-}$ in the presence of water to give H_2O_2 and Cu^{2+}, as given in equation (iv). These reactions take place in a cyclic manner as long as $O_2^{\bullet-}$ is available at the surface of the electrode, resulting in a linear response in the current. In addition to the enzyme-mimicking activity, the combination of CuONP and ZTF-8 results in the formation of heterostructures, which would generate a larger number of catalytically active sites, facilitating the electrocatalytic reduction and analytical performance towards the detection of $O_2^{\bullet-}$.

3.5 Evaluation of the Michaelis–Menten parameters

The Michaelis–Menten constants (K_m & I_{max}) provide crucial directives regarding the enzyme-substrate affinity and are hence regarded as highly vital in probing the catalytic properties of enzyme-based systems. A lesser K_m and greater I_{max} values indicate an efficient substrate and enzyme binding, which would proficiently enhance the enzymatic activity. Therefore, while fabricating an enzyme-mimic, these parameters aid in a clear understanding of the nanozyme behaviour. Herein, the SOD-mimicking characteristics of CuO/ZTF-8 were evaluated using the Lineweaver–Burk equation given below:

$$\frac{1}{I} = \frac{K_m}{I_{max}}\frac{1}{C} + I_{max}$$

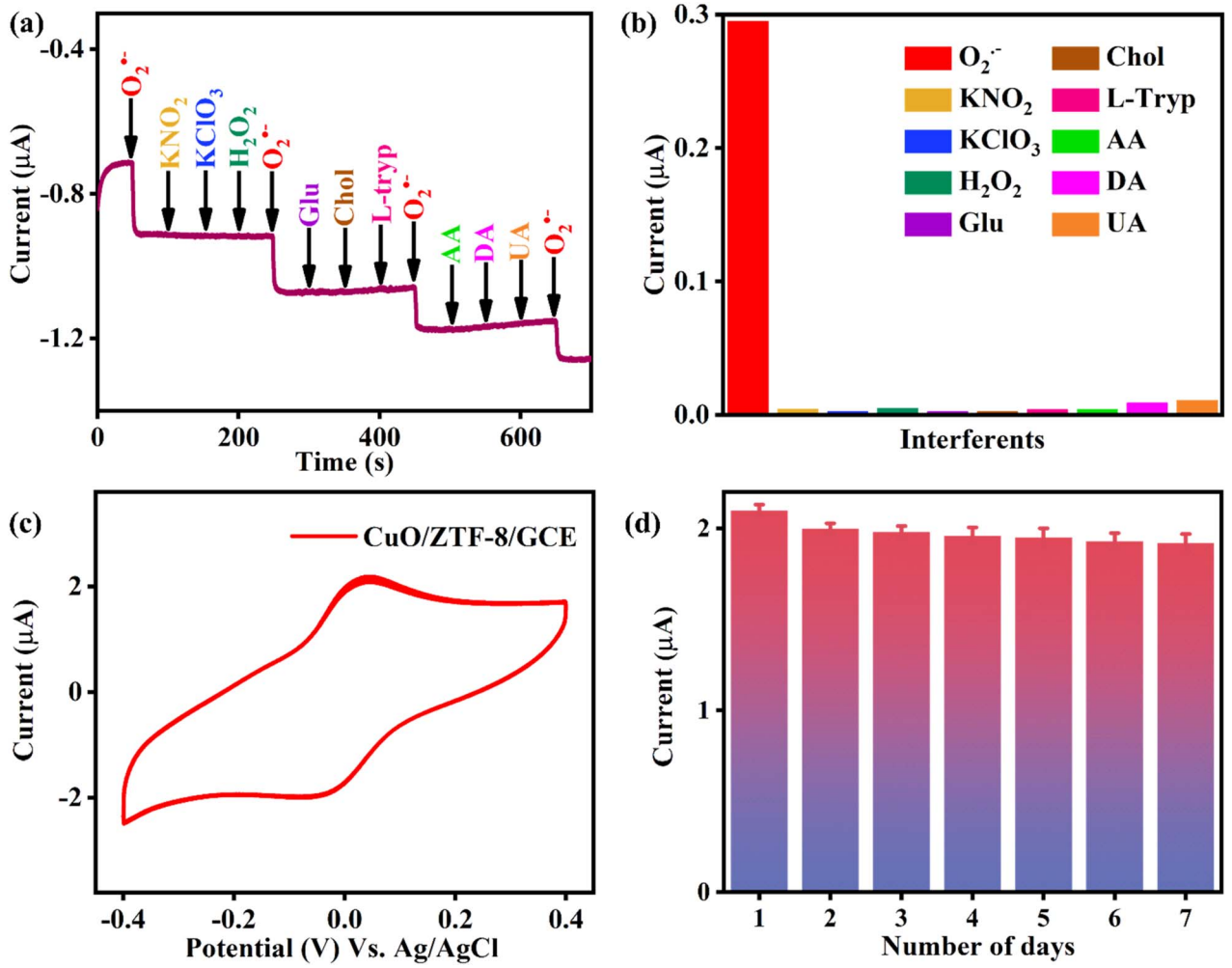

Fig. 6 (a) Effect of interfering species on the amperometric (*i*–*t*) current response of the CuO/ZTF-8/GCE for 25 μM $O_2^{\bullet-}$ in 0.1 M phosphate buffer (pH 7; N_2 saturated). (b) Corresponding columnar current response. (c) Cyclic voltammogram of CuO/ZTF-8/GCE at a scan rate of 50 mV s^{-1} in 0.1 M phosphate buffer (pH 7, N_2 saturated) for 100 continuous cycles. (d) Columnar diagram of the current response obtained for CuO/ZTF-8/GCE from CV studies for seven consecutive days.

where I is the anodic/cathodic current, C is the analyte concentration, and I_{max} is the maximum electrocatalytic current. The K_m and I_{max} values were determined using the plot of $1/I$ *versus* $1/C$ of $O_2^{\bullet-}$ (Fig. 5d) and were found to be 1.6 mM and 6.33 μA, correspondingly. These significantly lower values obtained for the CuO/ZTF-8 nanocomposite suggests that the CuO/ZTF-8 architecture could potentially replace the natural Cu–Zn SOD enzyme in sensing applications.

3.6 Effect of interferents and stability

The effect of interferents towards the electrochemical detection of $O_2^{\bullet-}$ was probed by carrying out amperometry tests in 0.1 M phosphate buffer (pH 7, N_2 saturated), at an operating potential of −0.2 V. Fig. 6a portrays the amperometric (i–t) responses of CuO/ZTF-8/GCE for $O_2^{\bullet-}$, in the presence of 10-fold excess of other interfering species, such as potassium nitrite (KNO_2), potassium perchlorate ($KClO_3$), H_2O_2, glucose (Glu), cholesterol (Chol), tryptophan (L-Tryp), ascorbic acid (AA), dopamine (DA), and uric acid (UA). Interferents like $KClO_3$, KNO_2, L-Tryp, and H_2O_2 were chosen due to their high tendency to interfere with $O_2^{\bullet-}$ sensing, at an applied potential of −0.2 V. Though DA, UA, AA, Chol, and Glu do not undergo reduction, these are commonly available interferents in biological systems and may interfere with $O_2^{\bullet-}$. The columnar diagram of the corresponding current response (Fig. 6b) shows that the fabricated CuO/ZTF-8/GCE was highly selective towards $O_2^{\bullet-}$. Herein, the selectivity of the CuO/ZTF-8 towards $O_2^{\bullet-}$ could be due to the bioinspired design of the nanocomposite. The CuO/ZTF-8 nanocomposite was designed to mimic the natural enzyme Cu–Zn SOD, where the CuONPs tend to serve as the catalytic site and the ZTF-8 host firmly anchors the CuONPs. Thus, the obtained heterostructure subsequently showed promising selectivity towards $O_2^{\bullet-}$.

Furthermore, the stability of the CuO/ZTF-8/GCE was studied by performing CV at a scan rate of 50 mV s^{-1} in 0.1 M PBS (pH 7, N_2 saturated) for 100 continuous cycles, and it was found that the sensor presented negligible change in current, inferring the robustness of the sensor (Fig. 6c). The surface of the GCE (after 3 batches of analysis) was scratched with the help of a needle and then the sample was subjected to PXRD studies (Fig. S10†). Notably, the major peaks at 7.8°, 35.3°, 38.6° of the (011), (002), and (111) facets corresponding to CuO/ZTF-8 were retained after 3 batches of analysis, corroborating that the composition of CuO/ZTF-8 remained almost the same, even after the catalytic reactions, thereby justifying the mechanisms proposed in Section 3.4. Additionally, CuO/ZTF-8/GCE was also tested for its reproducibility using CV in 0.1 M PBS (pH 7, N_2 saturated) for seven days, and the results are presented in Fig. 6d. This figure reveals that the fabricated sensor was stable for seven days, which suggests the excellent reproducibility of the constructed sensor. The extraordinary stability of the sensor design was attributed to the firm CuO/ZTF-8 heterostructure obtained by the stable anchoring of the CuONPs in the robust zeolitic architecture.

Table 2 Real-time analysis of $O_2^{\bullet-}$ in bovine serum albumin samples

S. no.	Sample	Spiked (μM)	Found[a] (μM)	% Recovery
1	Serum	300	298.2 ± 1	99.6
2		600	614.3 ± 3	102.3

[a] Experiments were performed in triplicate.

3.7 Real-time analysis

The fabricated sensor was employed towards sensing $O_2^{\bullet-}$ in serum samples and the results are shown in Fig. S11.† Briefly, serum samples (1 mg mL^{-1}) were prepared using 0.1 M PBS (pH 7) and a known concentration of $O_2^{\bullet-}$ was spiked by the standard addition method. The fabricated sensor showed good recovery ranging from 99.6–102.3% (Table 2), demonstrating its practical applicability.

4. Conclusion

To summarise, a Cu–Zn SOD-mimicking novel CuO/ZTF-8 nanocomposite was designed and developed for the electrochemical detection of $O_2^{\bullet-}$. The CuO/ZTF-8 nanocomposite was drop-cast on a GCE to fabricate a CuO/ZTF-8/GCE sensor, which demonstrated admirable nanozyme activity towards the reduction of $O_2^{\bullet-}$. The constructed sensor functioned by reduction of $O_2^{\bullet-}$ which was achieved by the careful design of the nanocomposite, by which $O_2^{\bullet-}$ could be detected amperometrically at a low applied potential of −0.2 V. The sensor exhibited broad linear ranges of 25–350 μM and 350 μM to 2.475 mM, with a low detection limit of 6.19 μM. Moreover, the mechanism of the CuO/ZTF-8/GCE sensor is expected to be the same as that of the naturally existing Cu–Zn SOD enzyme. Furthermore, ZTF-8 served as an excellent host to anchor the CuONPs, whereby the resulting heterostructure would generate abundant catalytically active sites, which would trigger the analytical performance of the CuO/ZTF-8/GCE sensor. In summary, this work discloses a pristine and prudently designed CuO/ZTF-8 nanocomposite with good SOD-mimicking properties for the selective electrochemical detection of $O_2^{\bullet-}$. The current work sets the stage for the judicious design and structural engineering of novel biomimetic materials towards various emerging biocatalytic applications and biomedical devices.

Data availability

The data supporting this article have been included as part of the ESI.† The original files will be made available upon request.

Author contributions

Vadakke Purakkal Sruthi: conceptualization, methodology, investigation, validation, writing – original draft. Shafeeq Sarfudeen: methodology, writing – original draft. Tamas Panda: resources, investigation, supervision, writing – review & editing. Kathavarayan Themozhi: conceptualization, supervision, writing – review & editing. Sellappan Senthilkumar:

conceptualization, resources, supervision, project administration, writing – review & editing.

Conflicts of interest

There are no conflicts to declare.

Acknowledgements

The authors thank the central research facility (CRF) VIT for providing the instrumentation facilities.

References

1 M. Hayyan, M. A. Hashim and I. M. Alnashef, *Chem. Rev.*, 2016, **116**, 3029–3085.
2 X. J. Chen, A. C. West, D. M. Cropek and S. Banta, *Anal. Chem.*, 2008, **80**, 9622–9629.
3 J. C. Juarez, M. Manuia, M. E. Burnett, O. Betancourt, B. Boivin, D. E. Shaw, N. K. Tonks, A. P. Mazar and F. Doñate, *Proc. Natl. Acad. Sci. U. S. A.*, 2008, **105**, 7147–7152.
4 C. M. C. Andrés, J. M. Pérez de la Lastra, C. Andrés Juan, F. J. Plou and E. Pérez-Lebeña, *Int. J. Mol. Sci.*, 2023, **24**, 3.
5 Y. Sheng, I. A. Abreu, D. E. Cabelli, M. J. Maroney, A. F. Miller, M. Teixeira and J. S. Valentine, *Chem. Rev.*, 2014, **114**, 3854–3918.
6 J. J. P. Perry, D. S. Shin, E. D. Getzoff and J. A. Tainer, *Biochim. Biophys. Acta, Proteins Proteomics*, 2010, **1804**, 245–262.
7 V. Lobo, A. Patil, A. Phatak and N. Chandra, *Pharmacogn. Rev.*, 2010, **4**, 118–126.
8 L. Gao, J. Zhuang, L. Nie, J. Zhang, Y. Zhang, N. Gu, T. Wang, J. Feng, D. Yang, S. Perrett and X. Yan, *Nat. Nanotechnol.*, 2007, **2**, 577–583.
9 Y. Huang, J. Ren and X. Qu, *Chem. Rev.*, 2019, **119**, 4357–4412.
10 D. Jiang, D. Ni, Z. T. Rosenkrans, P. Huang, X. Yan and W. Cai, *Chem. Soc. Rev.*, 2019, **48**, 3683–3704.
11 H. Wei and E. Wang, *Chem. Soc. Rev.*, 2013, **42**, 6060–6093.
12 B. Das, J. Lou Franco, N. Logan, P. Balasubramanian, M. Il Kim and C. Cao, *Nano–Micro Lett.*, 2021, **13**, 193.
13 Y. Lin, J. Ren and X. Qu, *Acc. Chem. Res.*, 2014, **47**, 1097–1105.
14 X. Wang, H. Wang and S. Zhou, *J. Phys. Chem. Lett.*, 2021, **12**, 11751–11760.
15 X. Niu, X. Li, Z. Lyu, J. Pan, S. Ding, X. Ruan, W. Zhu, D. Du and Y. Lin, *Chem. Commun.*, 2020, **56**, 11338–11353.
16 C. Guo, F. Duan, S. Zhang, L. He, M. Wang, J. Chen, J. Zhang, Q. Jia, Z. Zhang and M. Du, *J. Mater. Chem. A*, 2022, **10**, 475–507.
17 D. Wang, D. Jana and Y. Zhao, *Acc. Chem. Res.*, 2020, **53**, 1389–1400.
18 X. Huang, S. Zhang, Y. Tang, X. Zhang, Y. Bai and H. Pang, *Coord. Chem. Rev.*, 2021, **449**, 214216.
19 T. Wu, S. Huang, H. Yang, N. Ye, L. Tong, G. Chen, Q. Zhou and G. Ouyang, *ACS Mater. Lett.*, 2022, **4**, 751–757.
20 F. Shi, Z. Shi, Z. Zou, X. Wu, Z. Liu, L. Liu, Q. Fu, Y. Li, W. Sun, C. Guo and C. M. Li, *ACS Appl. Nano Mater.*, 2022, **5**, 6268–6276.
21 Y. Ma, Y. Zhang and L. Wang, *Talanta*, 2021, **226**, 122105.
22 E. Saeb and K. Asadpour-Zeynali, *Electrochim. Acta*, 2022, **417**, 140278.
23 A. Paul, I. K. Banga, S. Muthukumar and S. Prasad, *ACS Omega*, 2022, **7**, 26993–27003.
24 T. Panda, P. Pachfule, Y. Chen, J. Jiang and R. Banerjee, *Chem. Commun.*, 2011, **47**, 2011–2013.
25 J. S. Qin, D. Y. Du, W. L. Li, J. P. Zhang, S. L. Li, Z. M. Su, X. L. Wang, Q. Xu, K. Z. Shao and Y. Q. Lan, *Chem. Sci.*, 2012, **3**, 2114–2118.
26 Y. Sun, F. Wang and J. Zhang, *Inorg. Chem.*, 2019, **58**, 4076–4079.
27 J. Liu, F. Wang and J. Zhang, *Cryst. Growth Des.*, 2017, **17**, 5393–5397.
28 F. Wang, Y. Liu, H. Zhang and K. Chu, *Chemcatchem*, 2019, **100083**, 1441–1447.
29 C. Qian, K. Han, W. Weng, Y. Zhang, W. Ma and Y. Song, *ChemistrySelect*, 2019, **4**, 5633–5640.
30 S. Sarfudeen, V. P. Sruthi, A. Maibam, P. Panda, P. Jhariat, S. Senthilkumar, R. Babarao and T. Panda, *Inorg. Chem.*, 2023, **62**, 20236–20241.
31 M. Yang, J. He, M. Hu, X. Hu, C. Yan and Z. Cheng, *Sens. Actuators, B*, 2015, **213**, 59–64.
32 S. Sarfudeen, P. K. Nitha, S. A. Basith, M. Varghese, P. Jhariat, A. Chandrasekhar and T. Panda, *ACS Appl. Mater. Interfaces*, 2024, **16**, 24851–24862.
33 M. I. Said, A. A. Othman and E. M. Abd Elhakeem, *RSC Adv.*, 2021, **11**, 37801–37813.
34 A. Devadoss, P. Sudhagar, C. Ravidhas, R. Hishinuma, C. Terashima, K. Nakata, T. Kondo, I. Shitanda, M. Yuasa and A. Fujishima, *Phys. Chem. Chem. Phys.*, 2014, **16**, 21237–21242.
35 Q. Song, S. K. Nataraj, M. V. Roussenova, J. C. Tan, D. J. Hughes, W. Li, P. Bourgoin, M. A. Alam, A. K. Cheetham, S. A. Al-Muhtaseb and E. Sivaniah, *Energy Environ. Sci.*, 2012, **5**, 8359–8369.
36 F. Yang, P. Song, X. Liu, B. Mei, W. Xing, Z. Jiang, L. Gu and W. Xu, *Angew. Chem.*, 2018, **57**, 12303–12307.
37 Y. Liang, T. Xia, Z. Wu, Y. Yang, Y. Li, Z. Sui, C. Li, R. Fan, X. Tian and Q. Chen, *Mater. Today Chem.*, 2022, **24**, 100777.
38 R. Zhu, J. Ding, J. Yang, H. Pang, Q. Xu, Q. Xu, D. Zhang and P. Braunstein, *ACS Appl. Mater. Interfaces*, 2020, **12**, 25037–25041.
39 Y. Zan, F. Ben Romdhane, A. Miche, C. Méthivier, J. M. Krafft, C. Jolivalt and J. Reboul, *ACS Appl. Mater. Interfaces*, 2023, **15**, 38716–38728.
40 C. Bonne, E. Latour, G. Modat, A. Muller, O. Palluy, J. B. Regnouf de Vains, G. Tissie and S. Veriac, *Bull. Soc. Chim. Belg.*, 1991, **9**, 673–676.
41 M. Zahirul Kabir, C. Erkmen, S. Kurbanoglu, G. Aydogdu Tig and B. Uslu, *J. Electroanal. Chem.*, 2023, **944**, 117651.
42 L. Qian, A. R. Thiruppathi, J. Van Der Zalm and A. Chen, *ACS Appl. Nano Mater.*, 2021, **4**, 3696–3706.
43 N. Mavis Xhakaza, R. Chokkareddy and G. G. Redhi, *J. Mol. Liq.*, 2022, **368**, 120444.
44 B. Derkus, E. Emregul and K. C. Emregul, *Talanta*, 2015, **134**, 206–214.

45 X. Zhu, X. Niu, H. Zhao, J. Tang and M. Lan, *Biosens. Bioelectron.*, 2015, **67**, 79–85.
46 Q. Qiu, H. Chen, Z. You, Y. Feng, X. Wang, Y. Wang and Y. Ying, *ACS Appl. Mater. Interfaces*, 2020, **12**, 5429–5436.
47 Q. Gao, H. Zhao, Z. Wang, X. Cai, L. Zhou and M. Lan, *Sens. Actuators, B*, 2021, **330**, 129309.
48 X. Liu, X. Liu, H. Wei, G. Song, H. Guo and X. Lu, *Sens. Actuators, B*, 2017, **252**, 503–510.
49 L. Wang, W. Wen, H. Xiong, X. Zhang, H. Gu and S. Wang, *Anal. Chim. Acta*, 2013, **758**, 66–71.
50 X. Wang, M. Han, J. Bao, W. Tu and Z. Dai, *Anal. Chim. Acta*, 2012, **717**, 61–66.
51 T. Ohsaka, Y. Tian, M. Shioda, S. Kasahara and T. Okajima, *Chem. Commun.*, 2002, **2**, 990–991.
52 Y. Wang, D. Wang, L. H. Sun, P. Xue, M. Q. Wang, Z. Lu, F. Wang, Q. Xia, M. W. Xu and S. J. Bao, *Biosens. Bioelectron.*, 2019, **133**, 133–140.
53 X. Cai, L. Shi, W. Sun, H. Zhao, H. Li, H. He and M. Lan, *Biosens. Bioelectron.*, 2018, **102**, 171–178.
54 J. S. Valentine and D. M. De Freitas, *J. Chem. Educ.*, 1985, **62**, 983–990.
55 J. A. Tainer, D. C. Richardson, J. S. Richardson and E. D. Getzoff, *Nature*, 1983, **306**, 284–287.